

# Enhancing Efficiency and Stability of Tin-Based Perovskite Solar Cells Through the Addition of Nickel (II) Porphyrin Complex for Defect Passivation and Mitigation of Ion Migration

Tewodros Abebe Debele, Belarani Ojha, Sushil Kumar, Yu-Cheng Chen, Chen-Hsiung Hung,\* and Eric Wei-Guang Diau\*

The stability and efficiency of tin perovskite solar cells (TPSCs) are often decreasing with high-density defects occurring at the grain boundaries of the perovskite film and the heterojunction interfaces of hole-transport material (HTM) and poly(3,4-ethylenedioxythiophene) polystyrene sulfonate (PEDOT:PSS). Hence, this study addresses these challenges using nickel (II) meso amino octaethylporphyrin (NiNH<sub>2</sub> OEP) as an effective defect-passivating agent for the device fabricated through a two-step method with an inverted device architecture. The precursor solution contains NiNH<sub>2</sub> OEP porphyrin coating over PEDOT:PSS, where NiNH<sub>2</sub> OEP is self-assembled uniformly at the perovskite grain boundary and interface between perovskite and HTM. NiNH<sub>2</sub> OEP is protonated to form nickel (II) ammonium porphyrin ions (NiNH<sub>3</sub><sup>+</sup> OEP) to retard nonradiative charge recombination and inhibit ion migration that occurred through the high-density defect states to improve device stability and performance. Consequently, the TPSC device fabricated with NiNH<sub>2</sub> OEP unveils a remarkable power conversion efficiency of 9.6%. Moreover, the stability of the device shows a prominent improvement that maintains an initial efficiency of 90% for more than 6,000 h inside the glove box.

These advantageous characteristics facilitate the creation of perovskite solar cells (PSCs) through cost-effective, low-temperature, and straightforward solution-based processes,<sup>[6–12]</sup> which address the growing need for environmentally friendly and clean energy sources.<sup>[13–16]</sup> Lead halide PSCs, specifically MAPbI<sub>3</sub> (MA: methylammonium), demonstrated significant power conversion efficiencies (PCEs) ranging from 3.8% to 26.1% over the ensuing decades.<sup>[17–19]</sup> However, the inherent toxicity of lead (Pb) raised environmental and health concerns, prompting researchers to explore lead-free alternatives.<sup>[20–23]</sup> Elements such as tin (Sn), germanium (Ge), indium (In), copper (Cu), antimony (Sb), manganese (Mn), and bismuth (Bi) have incipient as environmentally acceptable substitutes for Pb in PSCs.<sup>[4,24–27]</sup>

Among these alternatives, tin-based PSC (TPSC) was the most promising lead-free option, with low toxicity, tunable bandgaps, high absorption coefficients, and small exciton binding energy.<sup>[28–32]</sup> Through the facile oxidation of Sn<sup>2+</sup> to Sn<sup>4+</sup>, easy degradation of film initiated from hygroscopic properties of the hole-transport material (HTM), poly(3,4-ethylenedioxythiophene) polystyrene sulfonate (PEDOT:PSS), poor morphology, fast crystallization, rapid nonradiative recombination, interfacial ion migrations,<sup>[25,33–38]</sup> and mismatch of energy levels has

## 1. Introduction

Solar cells based on perovskite (PSK) materials represent a burgeoning photovoltaic technology distinguished by its exceptional optoelectronic properties, such as an adjustable bandgap, extended diffusion length, tunable binding energy, good absorption coefficient, and admirable charge transport.<sup>[1–5]</sup>


high absorption coefficients, and small exciton binding energy.<sup>[28–32]</sup> Through the facile oxidation of Sn<sup>2+</sup> to Sn<sup>4+</sup>, easy degradation of film initiated from hygroscopic properties of the hole-transport material (HTM), poly(3,4-ethylenedioxythiophene) polystyrene sulfonate (PEDOT:PSS), poor morphology, fast crystallization, rapid nonradiative recombination, interfacial ion migrations,<sup>[25,33–38]</sup> and mismatch of energy levels has

T. A. Debele, Y.-C. Chen, E. W. G. Diau  
Department of Applied Chemistry and Institute of Molecular Science  
National Chiao Tung University  
1001 Ta-Hsueh Rd., Hsinchu 300093, Taiwan  
E-mail: diau@nycu.edu.tw

T. A. Debele, B. Ojha, S. Kumar, C.-H. Hung  
Institute of Chemistry  
Academia Sinica  
Nangang, Taipei 11529, Taiwan  
E-mail: chhung@gate.sinica.edu.tw

T. A. Debele  
Sustainable Chemical Science and Technology (SCST)  
Taiwan International Graduate Program (TIGP)  
Academia Sinica  
Nangang, Taipei 11529, Taiwan

E. W. G. Diau  
Center for Emergent Functional Matter Science  
National Chiao Tung University  
1001 Ta-Hsueh Rd., Hsinchu 300093, Taiwan

 The ORCID identification number(s) for the author(s) of this article can be found under <https://doi.org/10.1002/solr.202301084>.

DOI: 10.1002/solr.202301084

impeded their performance and stability.<sup>[39,40]</sup> To address these challenges, extensive efforts have been invested in interfacial engineering, solvent engineering, composition engineering, configurational structures, and an assortment of charge-transport layers (HTMs and electron-transport layer) materials.<sup>[13,41]</sup>

Metalloporphyrin molecules ( $\text{Zn}^{2+}$ ,  $\text{Cu}^{2+}$ ,  $\text{Co}^{2+}$ , and  $\text{Ni}^{2+}$ ), featured with high optoelectronic properties such as high charge carrier mobility, excellent light absorption, and superior thermal and chemical stability<sup>[42–44]</sup> that play pivotal roles as interfacial materials for TPSC. They give contributions of suppressing the defects through regulation of morphology, control rate of crystallinity, energy-level matching, intrinsic encapsulation, extraction of holes from the PSK lattice, and minimize charge recombination.<sup>[45–47]</sup> Subsequently, these interventions caused an increase in the open-circuit voltage ( $V_{oc}$ ), short-circuit currents ( $J_{sc}$ ), and fill factor (FF) of the device.<sup>[42,45–51]</sup>

In the present study, we dedicated significant efforts on the fabrication of TPSC with enhanced efficiency, remarkable stability, and environmental friendliness by addition of nickel (II) meso amino octaethylporphyrin ( $\text{NiNH}_2$  OEP) and its derivatives in the precursor solutions as the molecular structures illustrated in **Figure 1b–d**, into tin PSK precursor solution for the device fabrication process involved a sequential fabrication method (**Figure S1**, Supporting Information) with an inverted device architecture, ITO/PEDOT:PSS/PSK/ $\text{C}_{60}$ /BCP/Ag (**Figure 1a**). The introduced porphyrin molecules well organized along the grain boundary of PSK films and HTM (PEDOT:PSS) served to passivate the high-density defects across the boundary layer and to thoroughly mitigate ion migration across interfacial layer that addressed the hygroscopic properties of PEDOT:PSS as well as regulated the surface morphology, controlled rate of

crystallization, reduced nonradiative charge recombination, and ensured an energy-level match. As a result, the performance and stability have been significantly improved to achieve PCE of 9.6% for a device fabricated with  $\text{NiNH}_2$  OEP porphyrin compared to the devices prepared with porphyrins ( $\text{Ni}$  OEP) (8.9%), ( $\text{NiNO}_2$  OEP) (7.5%), and without porphyrin additive ( $\text{FASnI}_3$ , FA: formamidinium) (8.4%). Also, the stability of the device was improved and maintained 90% of its initial value over 6000 h.

## 2. Results and Discussion

### 2.1. Distribution Analysis of Porphyrin in Tin PSK Film

The dispersion analysis of tin PSK ions and  $\text{NiNH}_2$  OEP porphyrin inside the film was studied using time of flight-secondary ion mass spectroscopy (TOF-SIMS). The results are shown in **Figure 2a** depicting overall ion distributions for  $\text{I}^-$ ,  $\text{Sn}^{2+}$ ,  $\text{FA}^+$ ,  $\text{C}^+$ ,  $\text{NiNH}_2^+$ , and  $\text{NiC}_4\text{H}_9\text{N}^+$ , with corresponding ion depth profiles shown in **Figure S2a,b**, Supporting Information, and 3D ion fragmentation (**Figure S3a–e**, Supporting Information) for comparison. Based on these results, tin PSK ions ( $\text{I}^-$ ,  $\text{Sn}^{2+}$ , and  $\text{FA}^+$ ) were observed near the top surface of the film at a shallow depth, whereas the nickel (II) meso amino octaethylporphyrin ion ( $\text{C}^+$ ,  $\text{NiNH}_2^+$ ,  $\text{NiC}_4\text{H}_9\text{N}^+$ ) disseminated at the middle to bottom zone of the PSK film due to large particle size of the porphyrin.<sup>[52–54]</sup>

Li et al. elucidated the process of monoamine zinc porphyrin (ZnP) reacting and assembling to modify methylammonium ( $\text{MA}^+$ ) lead iodide PSK film.<sup>[55]</sup> This involved the amine group in ZnP reacting with  $\text{MA}^+$  and  $\text{I}^-$  ions, yielding

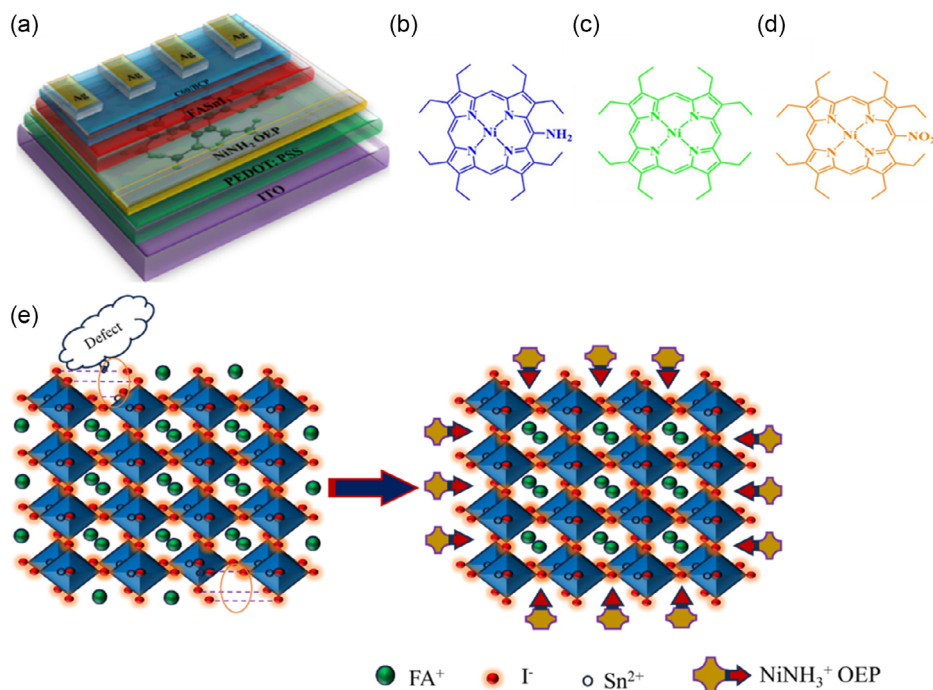


**Figure 1.** a) Schematic demonstration of a TPSC device configuration. b–d) Molecular structures of metalloporphyrin of  $\text{NiNH}_2$  OEP,  $\text{Ni}$  OEP, and  $\text{NiNO}_2$  OEP, respectively. e) The assembly coordination of PSK with  $\text{NiNH}_2$  OEP porphyrin as defects passivator.

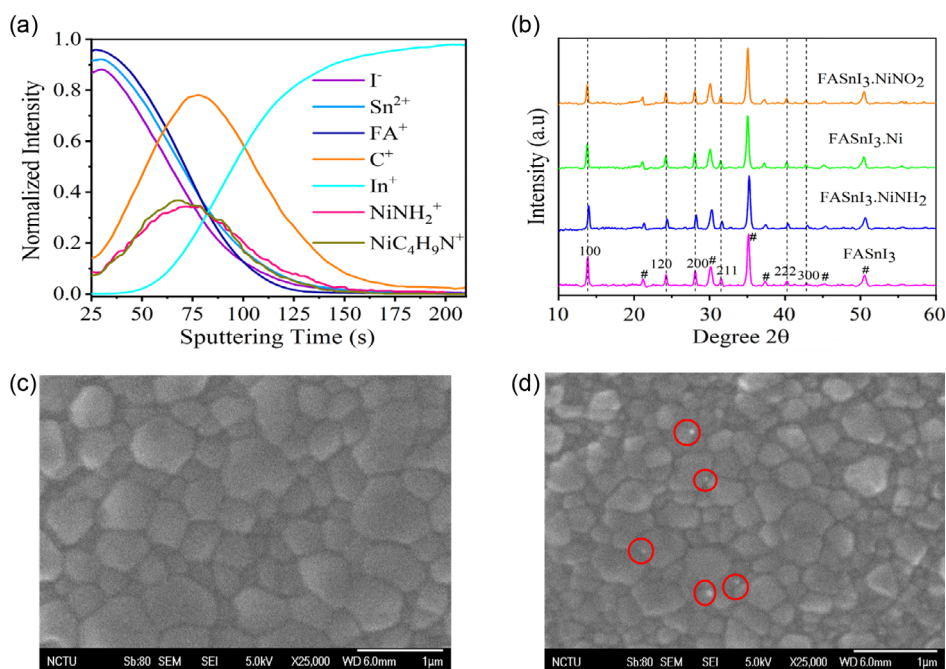


**Figure 2.** a) NiNH<sub>2</sub> OEP dispersion in TPSC film, b) XRD of TPSC film (# represents ITO), and SEM images of c) FASnI<sub>3</sub>-NiNH<sub>2</sub>OEP film and d) FASnI<sub>3</sub> film.

monoammonium zinc porphyrin (ZnP-H<sup>+</sup>I<sup>-</sup>), which in turn resulted in the retardation of ion migration through the formation of ZnP-H<sup>+</sup>I<sup>-</sup> bonds on the surface and grain boundary of the PSK film. Additionally, Fang and co-workers provided evidence of atomistic defects at grain boundaries, where the formation of cation-cation and anion-anion incorrect bonds led to a decrease in hole mobility within PSK grain boundaries.<sup>[50]</sup> This issue was addressed by the self-assembly of supramolecules of monoamine porphyrins to tailor organic cations (FA<sup>+</sup>) PSK at grain boundaries, forming ammonium porphyrin (MP-H<sup>+</sup>), which efficiently bound the supramolecules to PSK grain surfaces. This process successfully passivated the defects on the PSK grain surfaces, facilitating efficient hole extraction and transport at PSK grain boundaries.<sup>[55]</sup> Similarly, we expected that NiNH<sub>2</sub> OEP might link with the organic cation FA<sup>+</sup> inside PSK and protonated to form the ionic form, NiNH<sub>3</sub><sup>+</sup> OEP, which helped in PSK to passivate the defects at the grain boundary of the PSK layer and the interface between PSK and PEDOT:PSS as shown in Figure 1e. As a result, the charge recombination might be retarded, inhibiting FA<sup>+</sup> ion to escape to serve as natural encapsulation at an interfacial layer that ensured the stability of the PSK film and effectively extracted holes and transported through the path of the link of porphyrin.<sup>[50,51]</sup>

## 2.2. Crystallinity and Morphological Analysis of the Films

The further characterization of the films with X-Ray diffraction (XRD) spectra depicted in Figure 2b revealed the successful fabrication of distinct 3D crystallographic phases of tin PSK film with porphyrin compound, which had consistency with the

previous work of PSK film synthesized without porphyrin.<sup>[41,53,54]</sup> The identified crystal planes (100, 120, 200, 211, 222, 300) with corresponded angles (13.82°, 24.28°, 28.08°, 31.53°, 40.29°, 42.83°) are clearly shown as dashed lines in Figure 2b for each sample.

Additionally, NiNH<sub>2</sub> OEP porphyrin imparted notable improvements in film morphology, as displayed in the scanning electron microscope (SEM) images (Figure 2c), showing a pinhole-free surface, excellent uniformity, and a more compacted morphology than the film fabricated without porphyrin (Figure 2d). The better film uniformity plays a significant role on the device performance by enhancing the transport of charge carriers, reducing device hysteresis, less interfacial defects at the PSK/HTM interface and improving light harvesting efficiency of the film.<sup>[37,46,49–52]</sup> As a result, the atomic force microscope (AFM) image (Figure S4a, Supporting Information) depicted low surface roughness (12.8 nm) for the film containing porphyrin, in contrast to the pristine film with larger roughness (18.0 nm) (Figure S4b, Supporting Information).

## 2.3. Optical Properties of the Films

From the analysis of optical property of the PSK film, the bandgap was determined from UV-vis absorption spectra of the Tauc plots as illustrated in Figure 3a, resulting in the bandgap energies of 1.41, 1.40, 1.42, and 1.44 eV for FASnI<sub>3</sub>-NiNH<sub>2</sub> OEP, FASnI<sub>3</sub>, FASnI<sub>3</sub>-Ni OEP, and FASnI<sub>3</sub>-NiNO<sub>2</sub> OEP films, respectively. Explicitly, the added porphyrin molecules did not alter the optical properties of the PSK films too much.<sup>[49,50,52]</sup> In photoluminescence (PL) spectra shown in Figure 3b, the slight blue spectral shift was observed for the film

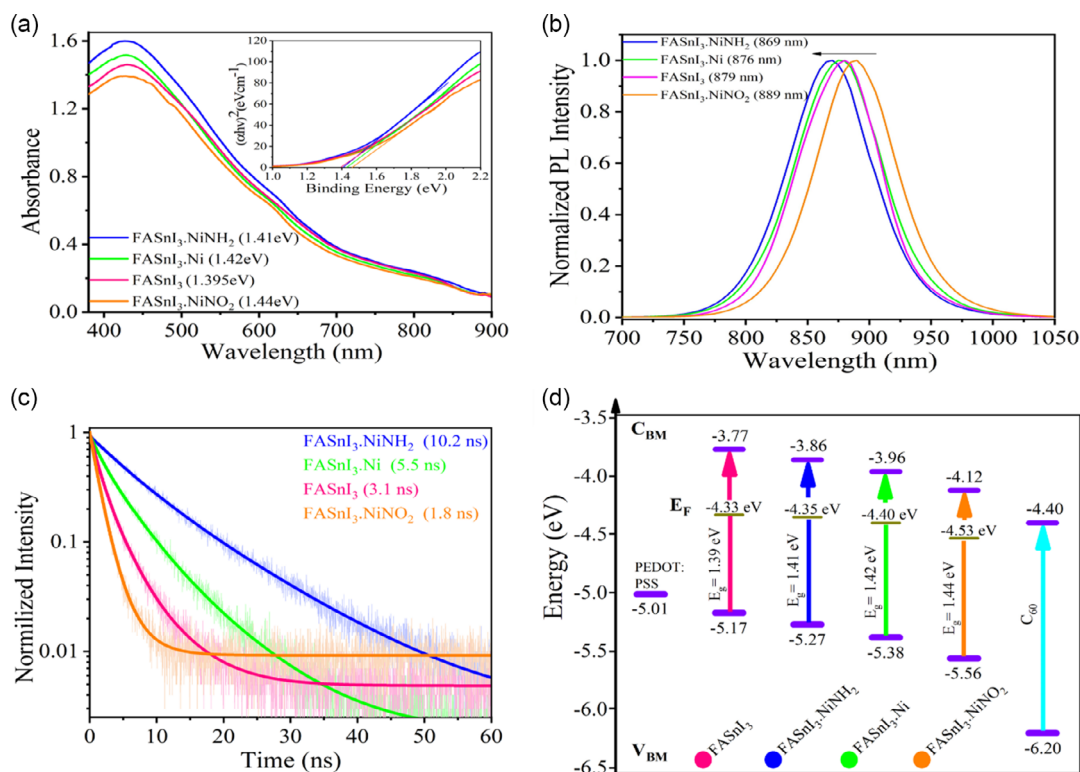


**Figure 3.** Optical properties for a) UV-vis absorption spectra, b) PL spectra, c) PL transient profiles obtained from TCSPC measurements, and d) energy-level diagram of tin PSK films as indicated.

with PSK compound with a donor group (FASnI<sub>3</sub>-NiNH<sub>2</sub> OEP) whereas the slight red spectral shift was found for that with an acceptor group (FASnI<sub>3</sub>-NiNO<sub>2</sub> OEP). The time-correlated single photon counting (TCSPC) measurements of the PSK films were carried out; the PL decay profiles are shown in Figure 3c; the corresponding PL lifetimes were calculated by fitting the data with a triexponential decay function;<sup>[48]</sup> the fitted time coefficients are summarized in Table S1, Supporting Information. The PSK film with NiNH<sub>2</sub> OEP porphyrin exhibited the largest PL lifetime (10.2 ns) compared to those of the FASnI<sub>3</sub>-Ni OEP (5.5 ns), FASnI<sub>3</sub> (3.1 ns), and FASnI<sub>3</sub>-NiNO<sub>2</sub> OEP (1.8 ns) samples. The longer PL lifetimes indicate the better effect of passivation on the grain boundaries to reduce the surface defect states. This explained as an effectively surpassed charge recombination<sup>[46-49]</sup> for the NiNH<sub>2</sub> OEP film than for the others. As a result, higher  $V_{oc}$  and FF values can be expected for the FASnI<sub>3</sub>-NiNH<sub>2</sub> device to enhance the overall cell performance and stability.<sup>[46-52]</sup>

Correspondingly, ultraviolet photoelectron spectroscopy (UPS) and UV/vis absorption spectra scrutinized the electronic structures to determine the energy levels for valence band maximum (VBM) and conduction band Minimum (CBM) of the PSK films. The UPS results are shown in Figure S5, Supporting Information, which determined VBM and Fermi levels for pristine FASnI<sub>3</sub>, FASnI<sub>3</sub>-NiNH<sub>2</sub> OEP, FASnI<sub>3</sub>-Ni OEP, and FASnI<sub>3</sub>-NiNO<sub>2</sub> OEP devices; the CBM levels were determined by adding the bandgaps to the CBM levels, as the energy-level results shown in Figure 3d. Typically, the PSK film with

porphyrin exhibited a higher VBM and a slightly wider bandgap than the pristine PSK film, which improved energy-level alignment and anticipated to enhance charge carrier collection and transport at the PSK/PEDOT:PSS interfaces, augmented in the overall photovoltaic performance.<sup>[47,49]</sup>

#### 2.4. X-Ray Photoelectron Spectroscopy Studies of the Films

To further illuminate the influence of porphyrin on the oxidation state ratio of tin (Sn<sup>2+</sup>/Sn<sup>4+</sup>), X-ray photoelectron spectroscopy (XPS) studies were carried out; the results are shown in Figure 4a-d with the proportions of the Sn<sup>2+</sup> and Sn<sup>4+</sup> species summarized in Table S2, Supporting Information. From the determination of the Sn<sup>2+</sup>/Sn<sup>4+</sup> ratio, the lowest value of Sn<sup>4+</sup> was obtained for the FASnI<sub>3</sub>-NiNH<sub>2</sub> OEP PSK film (3.8%), which is much lower than those of FASnI<sub>3</sub> (18.55%), FASnI<sub>3</sub>-Ni OEP (7.2%), and FASnI<sub>3</sub>-NiNO<sub>2</sub> OEP (23.4%) PSK films. This entailed that the NiNH<sub>2</sub> OEP porphyrin more effectively hampers the oxidation of Sn<sup>2+</sup> in the PSK film.<sup>[41,53,54]</sup>

#### 2.5. Device Performance, Stability, and Reproducibility

The device performances were measured with reverse scan mode of the current density-voltage ( $J-V$ ) characteristic via a solar simulator (AM1.5G, XES-40S1, SAN-EI) under ambient conditions at a scan rate of 0.02 V with the active cell area 0.0225 cm<sup>2</sup>. The  $J-V$  scan curves are presented in Figure 5a, and the corresponding photovoltaic parameters are listed in Table 1.



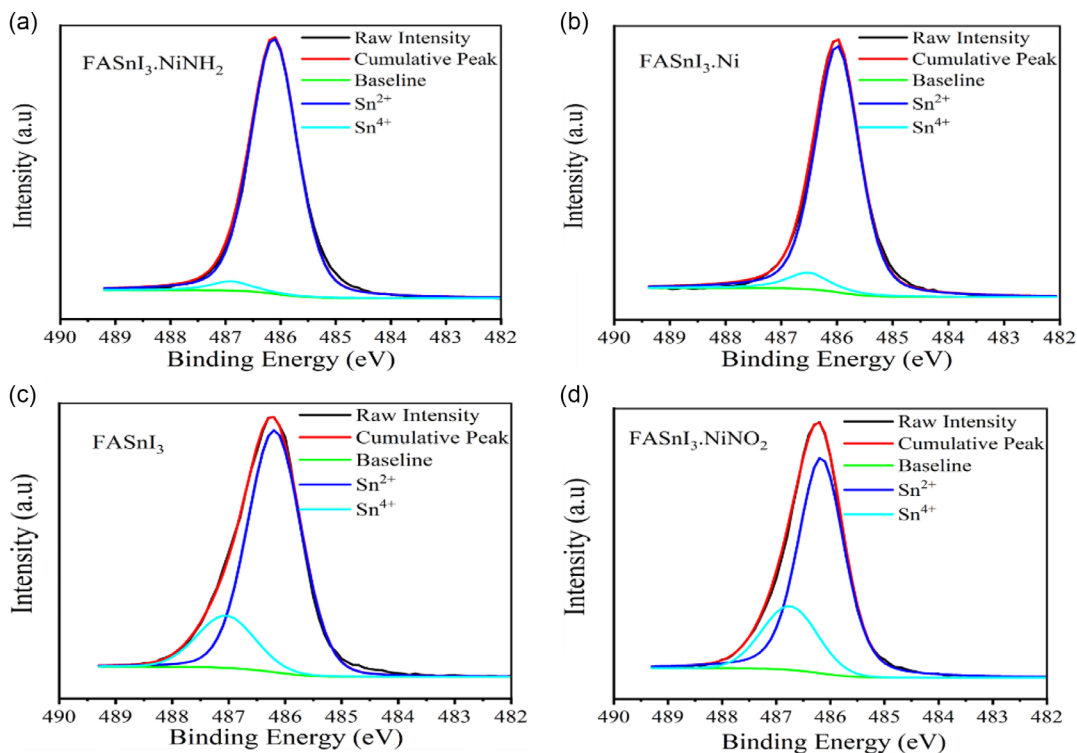


**Figure 4.** XPS spectra of tin PSK films of a) FASnI<sub>3</sub>-NiNH<sub>2</sub> OEP, b) FASnI<sub>3</sub>-Ni OEP, c) FASnI<sub>3</sub>, and d) FASnI<sub>3</sub>-NiNO<sub>2</sub> OEP.

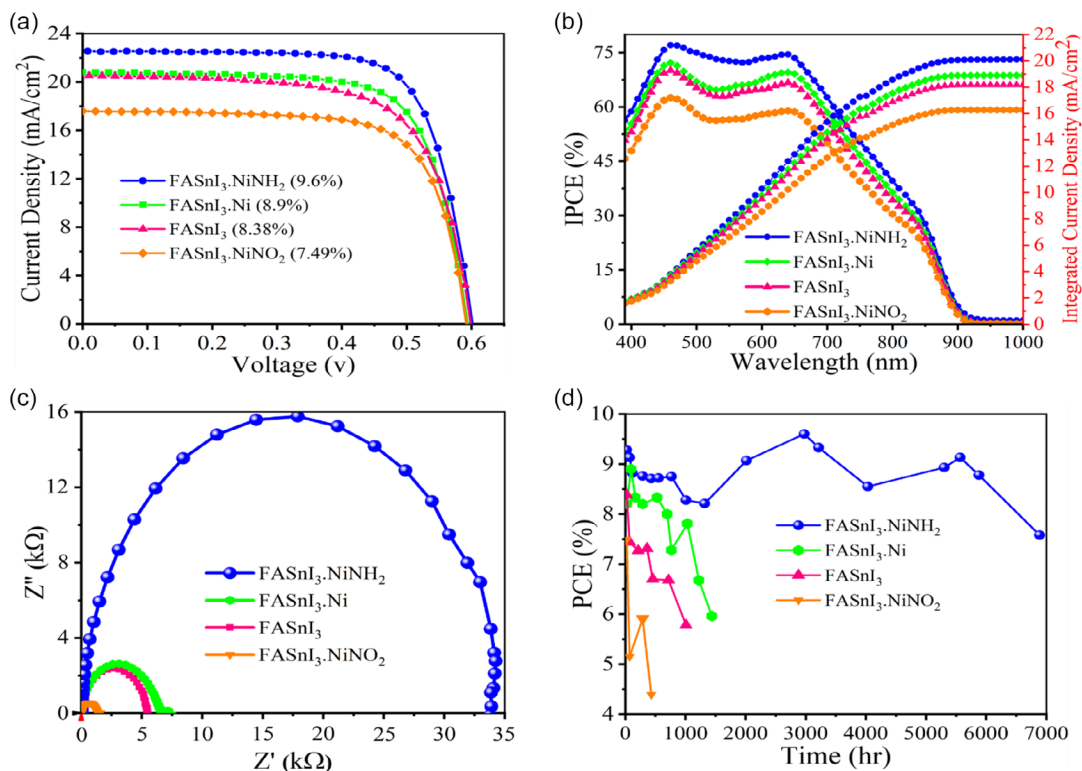


**Figure 5.** a) *J*-*V* curves, b) IPCE spectra of tin PSKs, c) Nyquist plots of PSK film obtained from EIS measurements with bias voltage 0.5 V, and d) performance stability of device.

**Table 1.** Photovoltaic parameters of TPSC device with and without the addition of porphyrin.

Device type	PCE [%]	$J_{sc}$ [ $\text{mA cm}^{-2}$ ]	$V_{oc}$ [V]	FF [%]
FASnI <sub>3</sub> -NiNH <sub>2</sub> OEP	9.6	22.20	0.600	72.10
FASnI <sub>3</sub> -Ni OEP	8.9	20.81	0.598	71.42
FASnI <sub>3</sub>	8.4	20.51	0.599	67.79
FASnI <sub>3</sub> -NiNO <sub>2</sub> OEP	7.5	17.58	0.597	71.25

The device fabricated with NiNH<sub>2</sub> OEP porphyrin exhibited the highest PCE (9.6%), which is significantly superior to the device made of pristine porphyrin FASnI<sub>3</sub> (8.4%). The FASnI<sub>3</sub>-Ni OEP device shows modest performance (8.9%), while the FASnI<sub>3</sub>-NiNO<sub>2</sub> OEP device shows the poorest performance (7.5%). To confirm the current density obtained from the  $J$ - $V$  scan measurements, we performed incident photon-to-current conversion efficiency (IPCE) spectra as shown in Figure 5b; the integrated current densities derived from IPCE spectra are consistent with those ( $J_{sc}$ ) obtained from the  $J$ - $V$  measurements (Figure 5a). In addition, the Nyquist plots (Figure 5c) obtained from the electrochemical impedance spectra (EIS) measurements explained the greatest charge recombination resistance for the FASnI<sub>3</sub>-NiNH<sub>2</sub> OEP device in comparison to the other devices. This demonstrated that the existence of NiNH<sub>2</sub> OEP porphyrin as an additive in TPSC has improved the interfacial charge extraction and transport<sup>[46,48,50,52]</sup> so that the charge recombination was retarded to give superior device performance than the others. Furthermore, the examination of hole-only space charge limited current (SCLC) for PSK device fabricated with porphyrin (NiNH<sub>2</sub> OEP) versus its pristine counterpart, as revealed in Supporting Information in Figure S6a, that resulted in higher hole mobility ( $\mu_{hole} = 2.38 \times 10^{-5} \text{ cm}^2 \text{ V}^{-1} \text{ s}^{-1}$ ) across the grain boundary layer of PSK and the interfacial layer between PSK and HTM (PEDOT:PSS) compared to the pristine device ( $\mu_{hole} = 1.44 \times 10^{-6} \text{ cm}^2 \text{ V}^{-1} \text{ s}^{-1}$ ). Additionally, the PSK film has porphyrin stemmed in a lower trap density ( $N_{trap} = 9.66 \times 10^{12} \text{ cm}^{-3}$ ) compared to the device without porphyrin ( $N_{trap} = 1.93 \times 10^{13} \text{ cm}^{-3}$ ), as shown in the Supporting Information in Figure S6b. To show the data reproducibility, the boxplots of 16 devices showing the statistical distributions of the device performance are provided in Figure S9, Supporting Information, and the corresponding photovoltaic parameters are given in Table S3–S6, Supporting Information.

We therefore conclude that treating the tin PSK film with the NiNH<sub>2</sub> OEP porphyrin molecule as an additive resulted in a significant improvement in promoting the device performance attributed to the mitigation of interface defects, suppression of ion migration, and prevention of moisture intrusion from PEDOT:PSS, which possesses hygroscopic property due to the hydrophobic nature of the porphyrin compounds. The hydrophobicity property has been confirmed with the analysis of water contact angle measurements for FASnI<sub>3</sub>-NiNH<sub>2</sub> OEP (65.24°) and pristine (51.20°) porphyrins as shown in Supporting Information in Figures S8a,b, respectively. Moreover, as depicted in Figure 5d, the PSK device produced with the NiNH<sub>2</sub> OEP porphyrin demonstrated remarkable stability by maintaining

over 90% of its initial PCE for a period exceeding 6000 h and maintained longer stability for the device kept at ambient conditions (relative humidity  $\approx 65\%$ ) as shown in Supporting Information in Figure S7a–c. In contrast, devices made of FASnI<sub>3</sub>-Ni OEP, FASnI<sub>3</sub>-NiNO<sub>2</sub> OEP, and pristine FASnI<sub>3</sub> PSKs exhibited much poor long-term stability compared to that of the FASnI<sub>3</sub>-NiNH<sub>2</sub> OEP device.

### 3. Conclusion

TPSCs were fabricated in a two-step procedure with porphyrin molecules (NiNH<sub>2</sub> OEP, Ni OEP, and NiNO<sub>2</sub> OEP) treated as surface passivation additive to improve the performance and stability of the devices. In particular, the introduced NiNH<sub>2</sub> OEP in the fabrication procedure of the PSK device has proved to be a key additive, yielding an efficient, stable, and reproducible device. The FASnI<sub>3</sub>-NiNO<sub>2</sub> OEP device achieved the highest PCE of 9.6% and sustained device efficiency exceeding 90% for shelf-storage in a glove box over 6000 h. The high performance of the NiNH<sub>2</sub> OEP device was attributed to its strong attachment to the surface of the PSK interacting with cation FA<sup>+</sup>, preventing cationic escape from tin PSKs. We also carried out comprehensive characterizations of related films and devices to understand their optical properties via UV-vis absorption, PL, and TCSPC measurements; morphological and crystalline features via SEM, AFM, and XRD measurements; and composition and electronic structure through TOF-SIMS, XPS, and UPS measurements, which reasonably account for their photovoltaic performances.

### 4. Experimental Section

**Materials:** This study used various types of chemicals and solvents such as tin iodide (SnI<sub>2</sub>) (99.999% Alfa Aesar), tin fluoride (SnF<sub>2</sub>) (Sigma-Aldrich), ethylenediammonium diiodide (EDA<sub>2</sub>) (Greatcell Solar), dimethyl sulfoxide (DMSO) (99.8% anhydrous, Sigma-Aldrich), formamidine iodide (FAI) (Greatcell Solar), isopropyl alcohol (IPA) (99.5% anhydrous, Sigma-Aldrich), 1,1,1,3,3,3-hexafluoro-2-propanol (HFP) (>99%, Sigma-Aldrich), chlorobenzene (CB) (Sigma-Aldrich), 2,9-dimethyl-4,7-diphenyl-1,10-phenanthroline (bathocuproine, BCP) (TCI), fullerene (C<sub>60</sub>) (UniRegion Bio-Tech), silver (Ag), and PEDOT:PSS (UniRegion Bio-Tech). These acquired chemicals and solvents were employed without undergoing additional purification. We utilized nickel metal complex porphyrins synthesized at the Academia Sinica Research Institute.

**Device Fabrication:** SnI<sub>2</sub> precursors solution containing nickel-metal porphyrin (NiNH<sub>2</sub> OEP/Ni OEP/NiNO<sub>2</sub> OEP) was used for device fabrication, which was prepared 1 day before the experiments. Indium tin oxide (ITO) glass substrate (1.9 cm  $\times$  1.9 cm) was first cleaned with a solvent containing IPA, acetone, and distilled water. Second, it was washed with only distilled water under a sonication bath for 30 min and dried in the oven. After the ITO glass substrate was treated in UV-ozone for about 20 min, PEDOT:PSS was coated over the substrate by spin coater at 5000 rpm for 50 s and annealed at 150 °C for 10 min. Then, PSK film was synthesized through two sequential processes inside nitrogen-filled glove box at the conditions of moisture <0.5 ppm and oxygen <0.2 ppm, starting with the coating of SnI<sub>2</sub> precursor solution chemical composition of [SnI<sub>2</sub> (1 mmol), SnF<sub>2</sub> (0.1 mmol), EDA<sub>2</sub> (0.01 mmol), NiNH<sub>2</sub> OEP/Ni OEP/NiNO<sub>2</sub> OEP (1.3% of SnI<sub>2</sub> wt/wt or 5 mg), and tin powder (50 mg)] mixed in DMSO (1.058 mL, PSK solution 0.95 M) deposited at 6000 rpm for 1 min and in succeeded FAI solution contains [FAI (20 mg) in a 5:5:2 ratio of solvent IPA (0.5 mL), HFP (0.5 mL), and CB (0.2 mL)] injected over SnI<sub>2</sub> precursor film and spin-coated at

5000 rpm for 12 s and then annealed at 70 °C for 10 min. Finally, tin PSK film was coated with electron-transport material (C<sub>60</sub>) at a thickness of (35 nm), hole-blocking material (BCP) (5 nm), and metal back-contact electrode (Ag) (100 nm) in the thermal evaporation at a pressure of  $5 \times 10^{-6}$  Torr.

**Device Characterization:** *J*–*V* characteristic curves were recorded by Keithley 2400 under 1 sun irradiation (AM1.5G, 100 mW cm<sup>-2</sup>) from a solar simulator (XES-40S1, SAN-E1) after calibrated with a silicon solar cell KG-5 filters and reverse scan (from *V*<sub>oc</sub> to 0 V) and forward scan (from 0 V to *V*<sub>oc</sub>), under ambient air conditions with metal mask area 0.0225 cm<sup>2</sup> and scan rate at 0.02 volt. The IPCE was measured with a system comprising a Xe lamp (A-1010, PTi, 150 W) and a monochromator (PTi, 1200 g mm<sup>-1</sup> blazed at 500 nm) after calibrated with a standard Si photodiode (S1337-1012BQ, Hamamatsu). EIS was obtained by an electrochemical workstation (IM 6, Zahner, Germany) over 100 mHz–4 MHz with an AC amplified amplitude of 10 mV under darkness at 0.3 V. The SCLC hole-only devices were fabricated with the structure of ITO/PEDOT:PSS/PSK/Al to investigate the trap density and hole mobility. *J*–*V* curves were measured from 0 to 6 V with a step size of 0.02 V under dark conditions using the *J*–*V* sweep mode on a Keithley 2400 source/meter unit.

(XRD) (Bruker D8 Advance and Cu K $\alpha$  radiation ( $\lambda = 1.5418 \text{ \AA}$ ) and SEM (Hitachi SU8010) and AFM (VT SPM, SII Nanotechnology Inc.) were used for analyzing the crystal and morphology of the PSK film, respectively. XPS elemental and the surface composition investigations were determined by Thermo K-alpha Surface Analysis machine, where XPS/UPS experiments were calibrated with the Fermi edge of the gold surface and performed in a high vacuum ( $\approx 10^{-9}$  Torr).

Optical properties were characterized by UV–vis (V780, Jasco) absorption, PL, and TCSPC (Fluotime 200, Picoquant) measurements with excitation at 635 nm for TCSPC. In addition, the composition and depth profile of thin films were analyzed by the TOF-SIMS (PHI TRIFT V nano TOF (ULVACPHI, Japan)) system via the dual-beam slice and view scheme.

## Supporting Information

Supporting Information is available from the Wiley Online Library or from the author.

## Acknowledgements

The authors thank Mr. Chiung-Chi Wang (Instrumentation Center, NTHU) for his assistance with TOF-SIMS measurements and gratefully acknowledge the support by the National Science and Technology Council (NSTC), Taiwan (grant nos. NSTC 111-2634-F-A49-007, NSTC 111-2123-M-A49-001, and NSTC 112-2639-M-A49-001-ASP) and the Center for Emergent Functional Matter Science of National Yang-Ming Chiao Tung University (NYCU) from the Featured Areas Research Center Program within the framework of the Higher Education Sprout Project by the Ministry of Education (MOE) in Taiwan.

## Conflict of Interest

The authors declare no conflict of interest.

## Data Availability Statement

Research data are not shared.

## Keywords

additives, hole-transport materials, interfacial layers, nickel porphyrins, tin perovskite solar cells

Received: December 31, 2023

Revised: February 15, 2024

Published online:

- [1] P. Tonui, S. O. Oseni, G. Sharma, Q. Yan, G. Tessema Mola, *Renewable Sustainable Energy Rev.* **2018**, *91*, 1025.
- [2] S. Dong, H. Yang, Z. Zhang, *Highlights Sci. Eng. Technol.* **2022**, *27*, 479.
- [3] J. H. Im, H. S. Kim, N. G. Park, *APL Mater.* **2014**, *2*, 081510.
- [4] H. Yao, F. Zhou, Z. Li, Z. Ci, L. Ding, Z. Jin, *Adv. Sci.* **2020**, *7*, 1903540.
- [5] W.-J. Yin, T. Shi, Y. Yan, W.-J. Yin, T. Shi, Y. Yan, *Adv. Mater.* **2014**, *26*, 4653.
- [6] Z. Chen, P. He, D. Wu, C. Chen, M. Mujahid, Y. Li, Y. Duan, *Front. Mater.* **2021**, *8*, 723169.
- [7] A. Chilvery, S. Das, P. Guggilla, C. Brantley, A. Sunda-Meya, *Sci. Technol. Adv. Mater.* **2016**, *17*, 650.
- [8] D. K. Jarwal, C. Dubey, K. Baral, A. Bera, G. Rawat, *IEEE Trans. Electron Devices* **2022**, *69*, 5012.
- [9] M. Mrinalini, N. Islavath, S. Prasanthkumar, L. Giribabu, *Chem. Rec.* **2019**, *19*, 661.
- [10] G. Giuliano, A. Bonasera, M. Scopelliti, D. Chillura Martino, T. Fiore, B. Pignataro, *ACS Appl. Electron. Mater.* **2021**, *3*, 1813.
- [11] J. W. Lee, N. G. Park, *MRS Bull.* **2015**, *40*, 654.
- [12] S. Ullah, J. Wang, P. Yang, L. Liu, S. E. Yang, T. Xia, H. Guo, Y. Chen, *Mater. Adv.* **2021**, *2*, 646.
- [13] E. W. G. Diau, E. Joker, M. Rameez, *ACS Energy Lett.* **2019**, *4*, 1930.
- [14] K. Hasan, S. Binti, Y. Mohammad, S. Hasan, K. Tushar, *Energy Sci. Eng.* **2022**, *10*, 656.
- [15] C. Lan, Z. Zhou, R. Wei, J. C. Ho, *Mater. Today Energy* **2019**, *11*, 61.
- [16] H. Mohammad, *Appl. Phys.* **2022**, *14*, 18.
- [17] Y. Zhou, L. M. Herz, A. K. Jen, M. Saliba, *Nat. Energy* **2022**, *7*, 794.
- [18] A. Mallick, I. Visoly-Fisher, *Mater. Adv.* **2021**, *2*, 6125.
- [19] W. J. Jang, H. W. Jang, S. Y. Kim, *Small Methods* **2023**, *8*, 2300207.
- [20] Y. Gao, Y. Hu, C. Yao, S. Zhang, *Adv. Funct. Mater.* **2022**, *32*, 2208225.
- [21] X. Jin, Y. Yang, T. Zhao, X. Wu, B. Liu, M. Han, W. Chen, T. Chen, J. Hu, Y. Jiang, *ACS Energy Lett.* **2022**, *7*, 3618.
- [22] J. Dou, Y. Bai, Q. Chen, *Mater. Chem. Front* **2022**, *6*, 2779.
- [23] J. Li, H. L. Cao, W. Bin Jiao, Q. Wang, M. Wei, I. Cantone, J. Lü, A. Abate, *Nat. Commun.* **2020**, *11*, 310.
- [24] T. J. Macdonald, L. Lanzetta, X. Liang, D. Ding, S. A. Haque, *Adv. Energy Mater.* **2023**, *35*, 2206684.
- [25] C. Ran, W. Li, H. Dong, Y. Zhou, W. Gao, Z. Wu, *ACS Appl. Energy Mater.* **2023**, *6*, 5102.
- [26] C. Wang, F. Gu, Z. Zhao, H. Rao, Y. Qiu, Z. Cai, G. Zhan, X. Li, B. Sun, X. Yu, B. Zhao, Z. Liu, Z. Bian, C. Huang, *Adv. Mater.* **2020**, *32*, 1907623.
- [27] N. Sun, W. Gao, H. Dong, Y. Liu, X. Liu, Z. Wu, L. Song, C. Ran, Y. Chen, *ACS Energy Lett.* **2021**, *6*, 2863.
- [28] C. Shih, C. Wu, *ACS Appl. Mater. Interfaces* **2022**, *14*, 16125.
- [29] P. Jiang, D. Acharya, G. Volonakis, M. Zacharias, M. Kepenekian, L. Pedesseau, C. Katan, J. Even, *APL Mater.* **2022**, *10*, 060902.
- [30] X. Jiang, Z. Zang, Y. Zhou, H. Li, Q. Wei, Z. Ning, *Acc. Mater. Res.* **2021**, *2*, 210.
- [31] R. Chandel, D. Deepak Punetha, D. Dhawan, N. Gupta, *Opt. Quantum Electron.* **2022**, *54*, 337.
- [32] T. Wu, X. Liu, X. He, Y. Wang, X. Meng, T. Noda, X. Yang, L. Han, *Sci. China Chem.* **2020**, *63*, 107.

- [33] Z. Jin, B. Bin Yu, M. Liao, D. Liu, J. Xiu, Z. Zhang, E. Lifshitz, J. Tang, H. Song, Z. He, *Energy Chem.* **2021**, *54*, 414.
- [34] H. Wang, B. W. Ang, B. Su, *Ecol. Econ.* **2017**, *142*, 163.
- [35] M. H. Futscher, M. Lee, L. Mcgovern, L. A. Muscarella, T. Wang, A. R. Fakharuddin, *RSC Mater. Horizons Commun.* **2019**, *6*, 1497.
- [36] E. Jokar, C. H. Chien, C. M. Tsai, A. Fathi, E. W. G. Diau, *Adv. Mater.* **2019**, *31*, 1804835.
- [37] B. Li, B. Chang, L. Pan, Z. Li, L. Fu, Z. He, L. Yin, *ACS Energy Lett.* **2020**, *5*, 3752.
- [38] Y. Zhao, W. Zhou, Z. Han, D. Yu, Q. Zhao, *Phys. Chem. Chem. Phys.* **2021**, *23*, 94.
- [39] T. Nakamura, S. Yakumar, M. A. Truong, K. Kim, J. Liu, S. Hu, K. Otsuka, R. Hashimoto, R. Murdey, T. Sasamori, H. Do Kim, H. Ohkita, T. Handa, Y. Kanemitsu, A. Wakamiya, *Nat. Commun.* **2020**, *11*, 3008.
- [40] Y. Su, J. Yang, G. Liu, W. Sheng, J. Zhang, Y. Zhong, L. Tan, Y. Chen, *Adv. Funct. Mater.* **2022**, *32*, 2109631.
- [41] C. H. Kuan, J. M. Chih, Y. C. Chen, B. H. Liu, C. H. Wang, C. H. Hou, J. J. Shyue, E. W. G. Diau, *ACS Energy Lett.* **2022**, *7*, 4436.
- [42] Y. Matsuo, K. Ogumi, I. Jeon, H. Wang, T. Nakagawa, *RSC Adv.* **2020**, *10*, 32678.
- [43] X. Zhang, S. Wang, W. Zhu, Z. Cao, A. Wang, F. Hao, *Adv. Funct. Mater.* **2022**, *32*, 2108832.
- [44] Y. C. Chin, M. Daboczi, C. Henderson, J. Luke, J. S. Kim, *ACS Energy Lett.* **2022**, *7*, 560.
- [45] J. E. Pia, B. A. Hussein, V. Skrypai, O. Sarycheva, M. J. Adler, *Coord. Chem. Rev.* **2021**, *449*, 214183.
- [46] K. Su, P. Zhao, Y. Ren, Y. Zhang, G. Yang, Y. Huang, Y. Feng, B. Zhang, *ACS Appl. Energy Mater.* **2021**, *13*, 14248.
- [47] B. Li, C. Zheng, H. Liu, J. Zhu, H. Zhang, D. Gao, W. Huang, *ACS Appl. Mater. Interfaces* **2016**, *8*, 27438.
- [48] C. Mai, Q. Zhou, Q. Xiong, C. Chen, J. Xu, Z. Zhang, H. Lee, C. Yeh, P. Gao, *Adv. Funct. Mater.* **2021**, *31*, 2007762.
- [49] X. Feng, Y. Huan, C. Zheng, C. Tan, H. Meng, B. Liu, D. Gao, W. Huang, *Org. Electron.* **2020**, *77*, 105522.
- [50] Z. Fang, L. Wang, X. Mu, B. Chen, Q. Wang, W. D. Wang, J. Ding, P. Gao, Y. Wu, J. Cao, *J. Am. Chem. Soc.* **2021**, *143*, 18989.
- [51] C. Li, J. Yin, R. Chen, X. Lv, X. Feng, Y. Wu, J. Cao, *J. Am. Chem. Soc.* **2019**, *141*, 6345.
- [52] K. Su, W. Chen, Y. Huang, K. G. Brooks, *Sol. RRL* **2022**, *6*, 2100964.
- [53] E. Jokar, C. H. Chien, A. Fathi, M. Rameez, Y. H. Chang, E. W. G. Diau, *Energy Environ. Sci.* **2018**, *11*, 2353.
- [54] M. Liao, B. Bin Yu, Z. Jin, W. Chen, Y. Zhu, X. Zhang, W. Yao, T. Duan, I. Djerdj, Z. He, *ChemSusChem* **2019**, *12*, 5007.
- [55] X. Li, C. Li, Y. Wu, J. Cao, Y. Tang, *Sci. China Chem.* **2020**, *63*, 777.